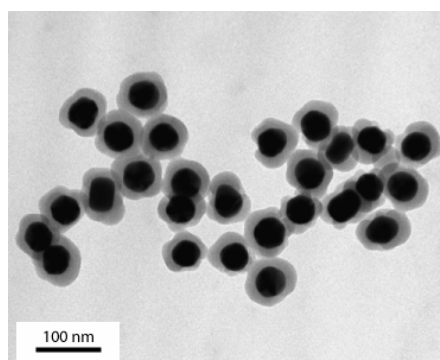
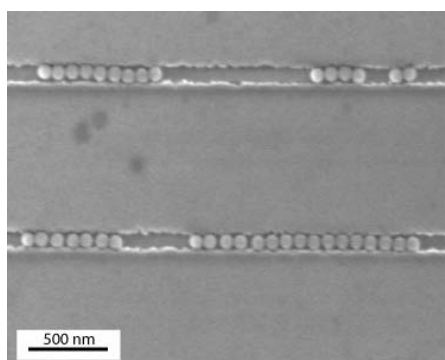
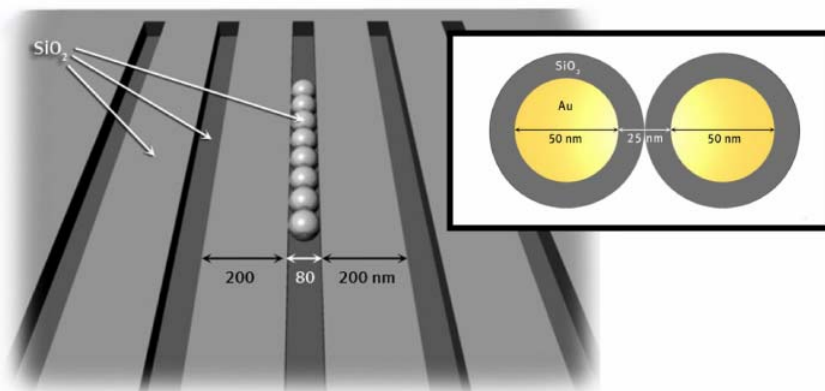


# Fabrication of plasmon waveguides by self-assembly

R. de Waele

Supervised by Drs. J. J. Penninkhof and Prof. Dr. A. Polman

In collaboration with Prof. Dr. A. van Blaaderen and Dr. A. M. Vredenberg



**Report of a research project performed in  
the period June 2004 – March 2005**

at



FOM-institute for Atomic and Molecular Physics  
Kruislaan 407, 1098 SJ Amsterdam, The Netherlands

and



Debye Institute, Utrecht University  
Padualaan 8, 3508 TA Utrecht, The Netherlands

## **Abstract**

Metal nanoparticle arrays can be used as waveguides to transport electromagnetic energy over short distances. For efficient dipole coupling of the plasmons the interparticle distance must be small: in case of 50 nm-diameter particles an interparticle distance of 25 nm is preferred. Such structures are very difficult to fabricate using conventional electron-beam lithography and lift-off techniques. Here, we study a new way to fabricate nanoparticle arrays by use of template-assisted self-assembly of colloids – an integration of lithography and self-assembly. Substrates were patterned with trenches and hole-arrays, using electron-beam lithography. It is shown that feature-sizes could be reduced by ion-beam irradiation of the template. Wet-chemically synthesized nanoparticles of silica and gold were self-assembled into the channels and holes to form arrays composed of 2-15 particles. Using core-shell colloids the interparticle distance in the Au particle array could be controlled by the thickness of the silica-shell.

## Table of contents

1	General introduction .....	1
1.1	Miniaturizing optical waveguides.....	1
1.2	Fabrication of plasmon waveguides.....	2
1.3	Thesis outline.....	3
2	Fabrication of templates for colloidal self-assembly .....	4
2.1	Introduction.....	4
2.2	Electron-beam lithography.....	4
2.3	Pattern-transfer to the substrate .....	6
2.4	Summary .....	8
3	Ion beam induced deformation of templates.....	9
3.1	Introduction.....	9
3.2	Experimental .....	9
3.3	Results and discussion .....	11
3.4	Conclusions.....	12
4	Synthesis of gold, silica and gold-core/silica-shell nanoparticles .....	13
4.1	Introduction.....	13
4.2	Silica nanoparticles .....	13
4.3	Gold nanoparticles .....	15
4.4	Gold-core/silica-shell nanoparticles.....	16
4.5	Conclusions.....	21
5	Template-assisted self-assembly of nanoparticles .....	23
5.1	Introduction.....	23
5.2	Silica nanoparticles .....	24
5.3	Gold nanoparticles .....	26
5.4	Gold-core/silica-shell nanoparticles.....	29
5.5	Conclusions.....	29
	Acknowledgements.....	30
	Reference list .....	31

# 1 General introduction

## 1.1 Miniaturizing optical waveguides

The manipulation of light is the key to many new and exciting optical applications for telecommunication, computing and sensing. Many of these devices require a high integration of optical components, which means that the light must be confined to very small dimensions. Today, light can be confined and manipulated at the micron and sub-micron scale using planar waveguides, optical fibers and photonic crystals. Optical fibers have the disadvantage that the guided energy cannot be steered around sharp corners with a bending radius smaller than the wavelength  $\lambda$  of the light [1]. Although light can be guided around sharp corners in photonic crystals, its minimal confinement is nevertheless restricted to the diffraction limit  $\lambda/2n$  of the light [2,3]. The diffraction limit can only be overcome, if the optical mode is somehow converted into a non-radiating mode that is confined to dimensions smaller than the diffraction limit.

Recently, it was proposed to use metals for the guiding of electromagnetic energy [4-8]. When a metal is exposed to light, a so-called surface plasmon can be excited. Plasmons are coherent oscillations of the free electrons in a metal. In case of small metal particles, the surface plasmons are strongly confined in three dimensions. The plasmon resonance frequency of these particles depends on several factors like size, shape and material. Both Au and Ag particles have been extensively studied, as their plasmon frequencies lie in the visible part of the spectrum. When the particles are much smaller than the wavelength of the exciting light, an oscillating dipole field is formed, resulting in a resonantly enhanced electromagnetic near-field close to the particle surface. When several particles are closely packed together in a 1-dimensional array, the near-fields of adjacent particles can couple, which allows for transport of electromagnetic energy below the diffraction limit [9, 10]. It has also been suggested that electromagnetic energy can be routed around sharp corners and T-junctions using these so-called plasmon waveguides [11].

Although the guiding of light along metal nanoparticle arrays is a great step forward toward the miniaturization of electromagnetic waveguides, propagation losses are very large in plasmon waveguides. For Au and Ag nanoparticles in air, energy decay lengths of only several hundred nanometer have been predicted [9]. It

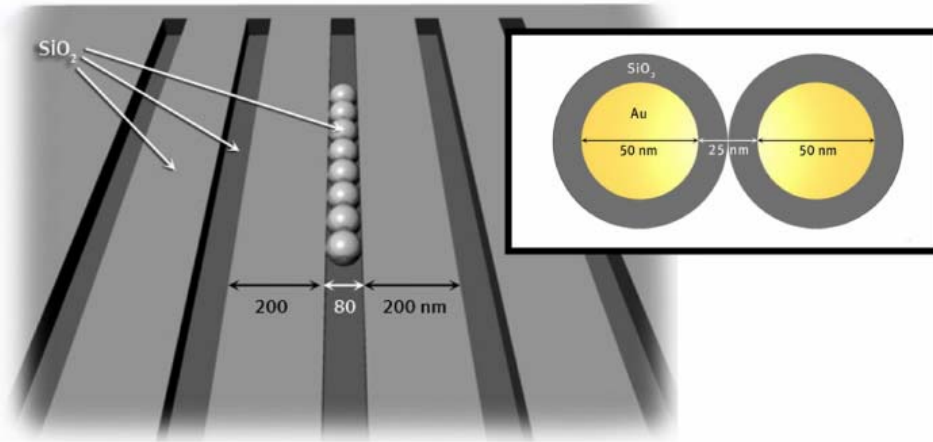


**Figure 1-1:** Schematic example of a plasmon waveguide formed by self-assembly of Au-core/silica-shell colloids in electron-beam defined trenches in silica. The inset shows a cross-section of two particles in the waveguide.

has been suggested that the propagation loss in plasmon waveguides can be reduced in several ways, for instance by using slightly elongated particles instead of spherical particles to form the array [12]. Although plasmon waveguides have recently received a great deal of attention, most of the research has been theoretical, while experiments involving plasmon waveguides are rare. We attempt to study the properties of plasmon waveguides experimentally.

## 1.2 Fabrication of plasmon waveguides

Plasmon waveguides consisting of metal nanoparticles can be fabricated using several methods. A few of the most promising are: (1) electron-beam lithography and lift-off; (2) electron/ion-beam induced deposition (EBID/IBID); (3) colloidal self-assembly. Using the first technique, plasmon waveguides have been successfully fabricated, and electromagnetic energy transport below the diffraction limit has been detected [10]. This method suffers from serious size-limitations, however. For efficient dipole coupling of the plasmons the interparticle distance must be small: in case of 50 nm-diameter particles an interparticle distance of 25 nm is preferred. Such structures are very difficult to fabricate using conventional electron-beam lithography and lift-off techniques. In EBID or IBID, metal nanoparticles are formed by electron-beam induced decomposition of a metallo-organic gas. Using this technique, nanoparticles

can be deposited with lateral sizes of 20-30 nm and an interparticle distance of  $\sim 10$  nm [13]. Drawbacks of this technique are the high equipment costs and slow fabrication. Colloidal self-assembly offers some great advantages over these techniques in terms of particle dimensions, fabrication time and costs, although the process is less controllable. Using this method, plasmon waveguides are formed by controlled drying of a colloidal dispersion over a electron-beam patterned substrate. By coating the metal particles with a dielectric material like silica, the interparticle distance in the particle array can be accurately tuned via the thickness of the shell. Figure 1-1 shows an schematic example of a self-assembled plasmon waveguide, consisting of Au-core/silica-shell nanoparticles.

### **1.3 Thesis outline**

In the following chapters, the fabrication of plasmon waveguides by self-assembly of metal nanoparticles in electron-beam defined patterns is discussed. Chapter 2 deals with the fabrication of templates, with feature sizes as small as  $\sim 30$  nm. In Chapter 3 is shown that these features can be further miniaturized by ion-beam irradiation of the template. The wet-chemical synthesis of silica, gold and gold-core/silica-shell nanoparticles is discussed in Chapter 4. Results of the self-assembly of these nanoparticles on fabricated templates are presented in Chapter 5.

## **2 Fabrication of templates for colloidal self-assembly**

### **2.1 Introduction**

Various areas in research and technology today rely on lithographic techniques for the patterning of materials with micro– and nanometer sized features. The oldest lithographic technique that is still in use in science and industry is photolithography which was invented in the 1950s. In photolithography a light-sensitive resist layer is exposed to visible or ultraviolet light through a patterned mask. The exposed material undergoes a chemical change which makes it either dissolvable in a developer solution, in case of a positive resist, or insoluble, in case of a negative resist. Even though photolithography is a relatively inexpensive and fast way to pattern a surface, features are limited in size by the wavelength of the light, to a typical size of  $\sim 90$  nm. This limitation has led to the development of techniques like x-ray lithography and electron-beam lithography.

In electron-beam lithography, a pattern is written directly in the resist without the use of a mask. Electron-beam lithography offers higher patterning resolution than optical lithography because of the shorter wavelength ( $\lambda \sim 0.2\text{--}0.5$  Å) possessed by the 10-50 keV electrons in the beam. The resolution is mainly limited by electron scattering, which occurs as the electrons interact with the atoms in the resist. This causes a widening of the diameter of the incident electron-beam as it penetrates the resist layer and also gives unintended extra doses of electron exposure as back-scattered electrons from the substrate bounce back to the resist. Another limiting factor for the resolution is the tendency of the polymer resist to swell in the developer solution.

### **2.2 Electron-beam lithography**

Using electron-beam lithography, patterns were defined in a PMMA layer on silica substrates. The substrates (size  $2 \times 2$  cm) were sawn out of a 500  $\mu\text{m}$ -thick circular quartz wafer (University Wafer,  $\varnothing = 10$  cm). After sonication (Branson 2510, 130 W) for 5 minutes in demiwater the substrates were transferred to a 5:1:1 volume mixture of demiwater, ammonium hydroxide (Merck, 33 wt.%) and hydrogen peroxide (Merck, 30 wt.%) and cleaned for 15 minutes at a temperature of  $75^\circ\text{C}$ . After thorough rinsing with demiwater the substrates were immersed in 2-propanol (Merck,

**Table 2-I:** Process details for several patterns in electron-beam lithography

pattern <sup>a</sup>	defined linewidth (nm)	dose ( $\mu\text{C}/\text{cm}^2$ )
30-50 nm lines	20	1050-1600
50-60 nm lines	30	900-1100
60-80 nm lines	60	480-780
1D hole array (30 nm)	-	250
2D hole array (50 nm)	-	95

<sup>a</sup> After transfer to the silica substrate.

p.a.) for 1 minute and dried in a nitrogen gas flow. The clean substrates were spin-coated (Süss Microtec Delta 10) at 4000 rpm for 55 seconds with a solution of 2 wt.% PMMA (MicroChem Corp., 950k) in chlorobenzene (Merck, p.a.) and baked on a hotplate (Präzitherm) for 45 minutes at 175°C. The thickness of the PMMA-layer was determined using a KLA Tencor Alphastep 500 surface profiler, and was typically ~80 nm. Next, a 20 nm-thick conductive germanium-layer was evaporated on the spin-coated substrates at a rate of 0.1 nm s<sup>-1</sup> using a vacuum coater (at a current of ~150 A).

The various steps of the lithographic process and subsequent pattern transfer to the substrate are shown in Fig. 2-1. Patterns were defined in the PMMA-layer using an electron-beam pattern generator (Jeol JSM 6460, 30 kV). Three types of patterns were written: straight lines, 1-dimensional arrays of holes and 2-dimensional arrays of holes (a typical writing field was 60×60  $\mu\text{m}$ ). Straight lines were written using a small step size of 5 nm, while holes were written by a single exposure every 80 nm. Table 2-I gives an overview of several fabricated patterns and the parameters for electron-beam exposure. For line-patterns a higher dose generally gave somewhat better results in terms of line-edge roughness, but also caused a widening of the predefined line. The narrowest lines (~30 nm) were written with a dose of 1050  $\mu\text{C}/\text{cm}^2$  and a predefined width of 20 nm. At lower dose the grooves would not fully open during development of the PMMA. The widest lines (~370 nm) were written with a dose of 640  $\mu\text{C}/\text{cm}^2$  and a predefined width of 300 nm.

## 2.3 Pattern-transfer to the substrate

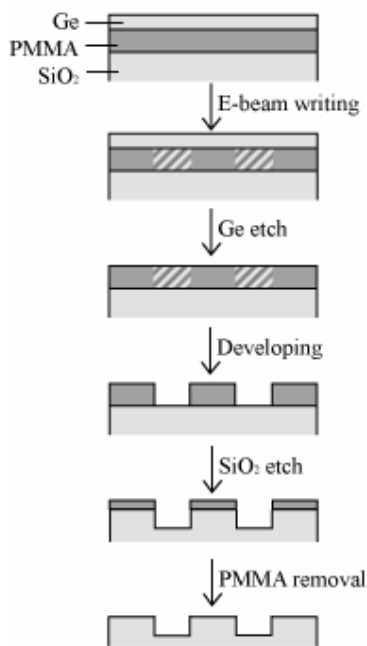


**Figure 2-1:** Schematic overview of the procedure to fabricate patterned silica substrates.

After electron-beam exposure the pattern in the PMMA layer was transferred to the SiO<sub>2</sub> substrate. First the germanium layer was removed with a SF<sub>6</sub>/O<sub>2</sub> plasma (Oxford Instruments Plasmalab 80+, 12.5 sccm SF<sub>6</sub>, 2.5 sccm O<sub>2</sub>, 40 W, 25 V, at 8 μbar, for ~45 s). Subsequently, the PMMA-layer was developed for 30 s using a 1:3 volume-mixture of methylisobutylketone and 2-propanol (MicroChem Corp.). Immediately after, the sample was immersed in 2-propanol for 15 s to stop the dissolution reaction, after which it was dried and stored.

The pattern was transferred to the substrate by anisotropic etching of SiO<sub>2</sub> with a 25 sccm CHF<sub>3</sub> / 25 sccm Ar plasma (RIE, 40 μbar). When the desired depth was reached (usually ~80 nm)

the sample was exposed to a 50 sccm O<sub>2</sub> / 50 sccm Ar plasma (RIE, 50 W, 220 V) to remove the PMMA layer. The etch rate and amount of line edge roughness in the transferred patterns were mainly determined by the choice of forward power during

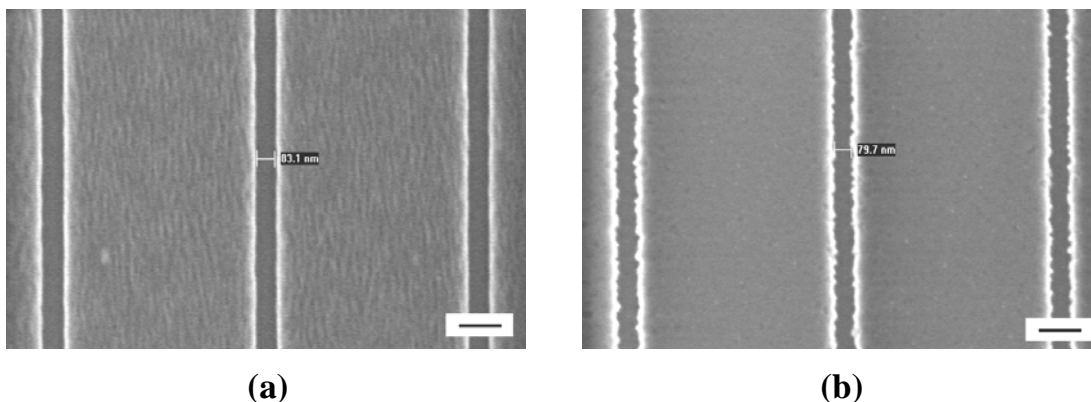
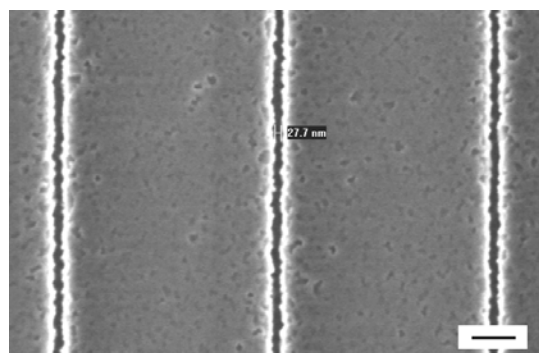
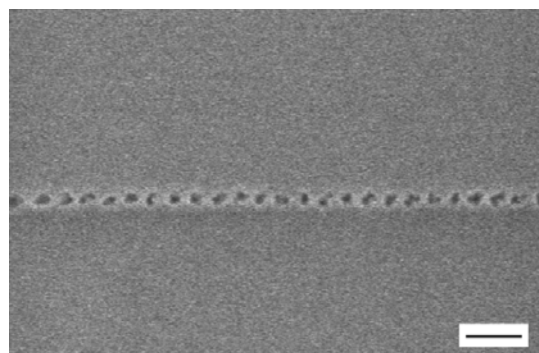


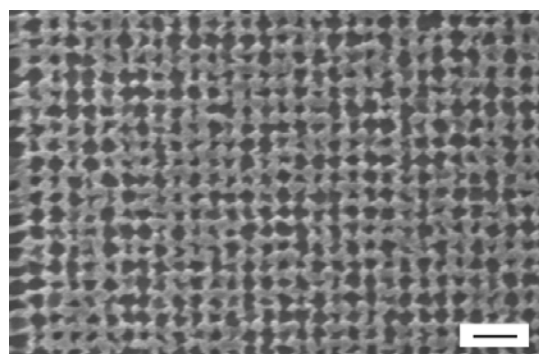
**Figure 2-2:** SEM images of silica templates after pattern transfer to the silica. (a) Silica etched using a forward power of 50 W. (b) Silica etched using a forward power of 300 W. Scale bars are 200 nm.



(a)



(b)



(c)

**Figure 2-3:** SEM images of several different patterns in silica. **(a)** Line-pattern with trench-widths of  $\sim 30$  nm. **(b)** 1-Dimensional hole pattern with holes of  $\sim 30$  nm and a pitch of 80 nm. **(c)** 2-Dimensional hole pattern with holes of  $\sim 50$  nm and a pitch of 80 nm. Scale bars are 200 nm.

nm-wide grooves, while the bottom two templates are patterned with holes of  $\sim 30$  nm (Fig. 2-3b) and  $\sim 50$  nm (Fig. 2-3c). An alternative way to write the hole pattern is by

the  $\text{SiO}_2$  etch. Figure 2-2 shows scanning electron microscope (SEM, FEI XL30 SFEG) images of two different substrates after pattern transfer. The left-side image in the figure shows a  $\text{SiO}_2$  sample that was etched at 50 W (etch rate  $8 \text{ nm min}^{-1}$ ). The sidewalls of the trenches are smooth in this case. Roughness of the sidewalls is much more pronounced for samples etched at 300 W (etch rate  $47 \text{ nm min}^{-1}$ ) shown in the right-side image of Fig. 2-2. During a reactive ion etch material is removed both through physical sputtering and chemical decomposition. As the forward power is increased sputtering becomes more important, which will in general lead to higher anisotropy but may also cause rougher sidewall features, because sputtering of material at the edge is limited by the presence of the PMMA mask.

Several examples of  $\text{SiO}_2$  templates are shown in Fig. 2-3. The template in the top image (Fig. 2-3a) is patterned with 30

exposure of small rectangles ( $20 \times 20$  nm) using a small step size. While this would probably give a nicer pattern, writing time would also increase dramatically.

## **2.4 Summary**

In this chapter, the used techniques to fabricate patterned substrates are discussed. Using electron-beam lithography a PMMA-layer was patterned and subsequently used as a mask for transfer of the pattern to a  $\text{SiO}_2$  substrate. Substrates containing 30 to 370 nm-wide trenches as well as linear arrays of holes have been prepared. These substrates were used as templates in controlled drying experiments of colloidal suspensions.

### **3 Ion beam induced deformation of templates**

#### **3.1 Introduction**

In the early 1980s Cartz *et al* discovered that small silicate particles could deform under MeV ion beams [14]. Intensive studies of this effect by others have led to a good understanding of the mechanism involved in the deformation [15-19]. When a colloidal silica particle is irradiated with ions it expands perpendicular and contracts parallel to the ion beam. The deformation of the colloid as a whole is caused by many microscopic changes as a result of individual ion impacts. When an ion penetrates a material it loses its energy both elastically through nuclear collisions and inelastically through excitation of electrons. The excited electrons can then transfer their energy to the lattice by electron-phonon coupling. As a result the material heats up considerably along the ion track, which can lead to the formation of a cylindrical molten region with a typical diameter of several nanometers. Shear relaxation resulting from the anisotropic stress, which is build up by the thermal expansion of the molten regions, is responsible for the ultimate deformation of the colloid.

Anisotropic deformation has also been observed for SiO<sub>2</sub> films with  $\mu\text{m}$ -wide trenches upon irradiation with 4 MeV Xe ions [20]. After irradiation the trenches had narrowed considerably. In this chapter we will discuss the deformation of 45-360 nm-wide trenches in silica.

#### **3.2 Experimental**

Using the techniques described in Chapter 2, a SiO<sub>2</sub> template was fabricated with six identical patterns spread out over the sample. A schematic overview of the sample after patterning is shown in Fig. 3-1. The patterns were all separated by more than 2 mm. Each of the six patterns contained eight fields of  $60 \times 60 \mu\text{m}$  consisting of linear arrays of trenches with a pitch of  $1 \mu\text{m}$ . The diameter of the trenches was fixed within each field, but varied between fields from 45 to 370 nm.

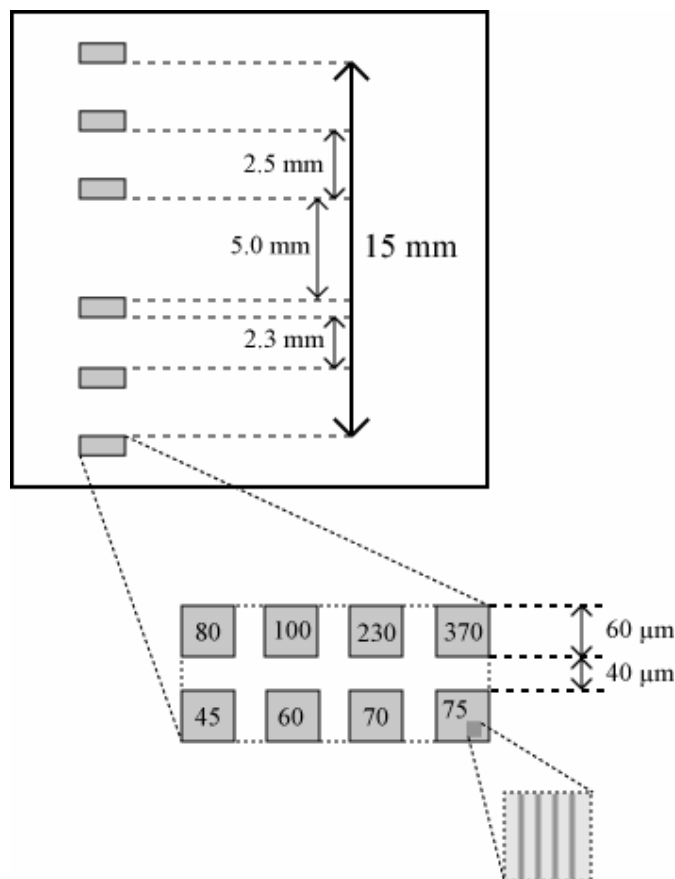


**Figure 3-1:** Schematic overview of the substrate before ion irradiation. All patterns contained eight fields with 45-370 nm-wide trenches written by electron-beam lithography. The fields had a size of  $60 \times 60 \mu\text{m}$  and the distance between fields was  $40 \mu\text{m}$ . The numbers in the fields represent trench-widths.

Next, the sample was irradiated with 6 MeV  $\text{Au}^{3+}$  ions using a 6 MV tandem accelerator. The chamber pressure during experiments was  $3 \times 10^{-7}$  mbar and the ion beam energy flux was kept constant at a value of  $0.1 \text{ W cm}^{-2}$ . The sample was clamped onto a copper stage that was cooled down using liquid nitrogen. The ion beam was scanned perpendicular to the sample surface across an area of  $1.0 \text{ cm}^2$ . By changing the vertical position of the stage, a pattern could be moved into or out of the ion beam. In this way the fluence could be varied between the patterns from  $5 \times 10^{13}$  to  $5 \times 10^{14} \text{ cm}^{-2}$ . One of the patterns was left unirradiated for reference. SEM was performed at an energy of 2 keV in order to characterize the trenches before and after irradiation of the template.

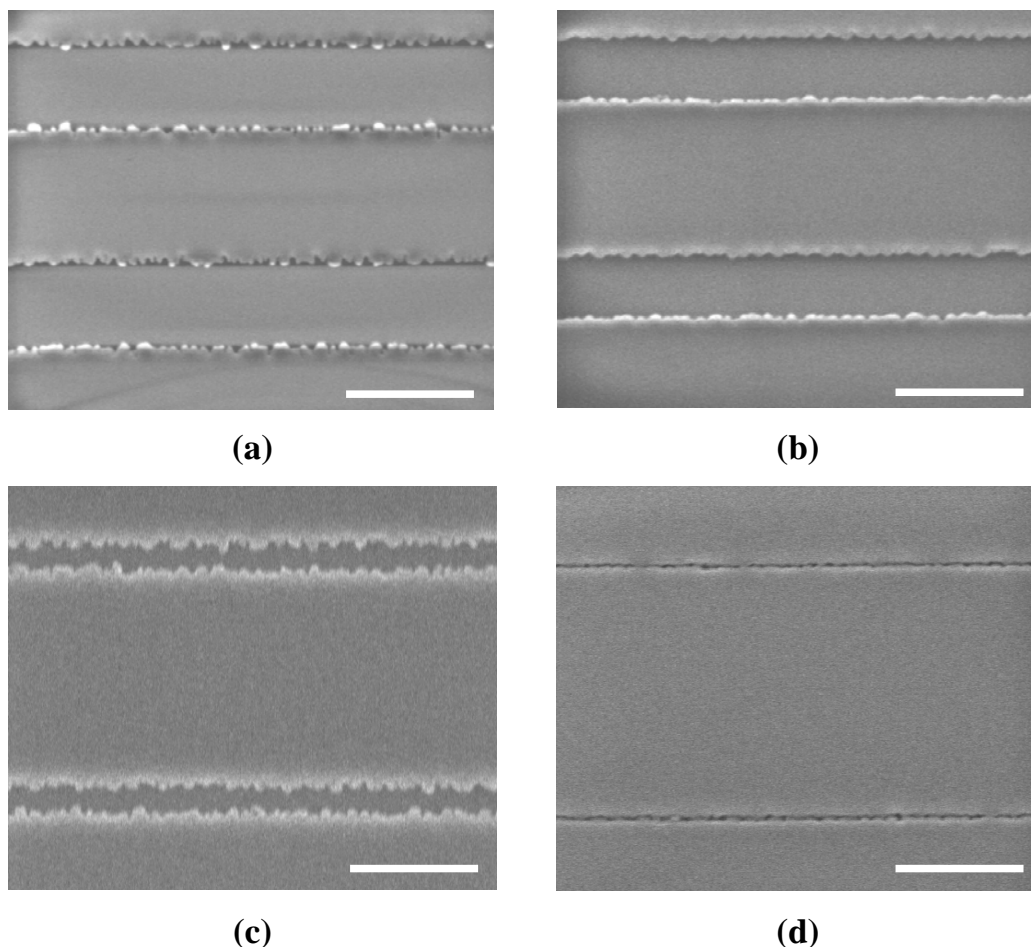


**Figure 3-2:** SEM images at the same magnification of templates before and after irradiation to a fluence of  $5 \times 10^{14} \text{ cm}^{-2}$  with the ion beam perpendicular to the substrate. **(a, c)** Unirradiated templates. **(b)** Template (a) after irradiation. **(d)** Template (c) after irradiation. Scale bars are 500 nm.

### 3.3 Results and discussion

Figure 3-2a shows a SEM image of a template before ion irradiation. The trenches in the figure have an mean width of  $373 \pm 15 \text{ nm}$ . After irradiation to a fluence of  $5.1 \times 10^{14} \text{ cm}^{-2}$  the trenches have a width of  $275 \pm 9 \text{ nm}$ . Line-edge roughness of the trenches did not seem improved after irradiation. Irradiation of trenches with a diameter of  $94 \pm 15 \text{ nm}$  (Fig. 3-2c) to the same fluence produces trenches with a diameter smaller than 10 nm (Fig. 3-2d).

In Fig. 3-3 the trench width vs. ion fluence is plotted for trenches with an initial width of 370, 230 and 100 nm. Deformation seems to take place at a somewhat higher

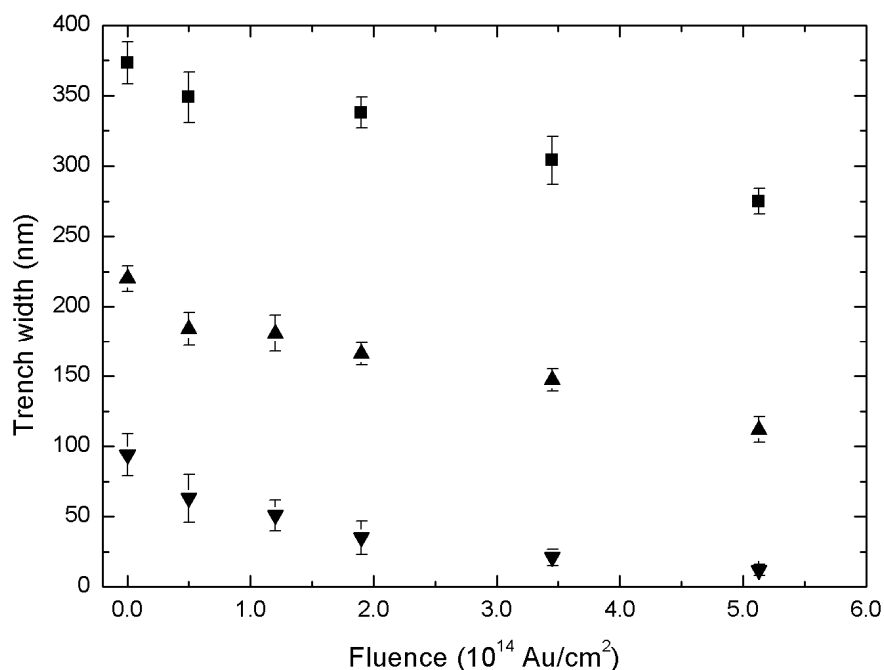


**Figure 3-3:** Trench width as a function of ion fluence for trenches with an initial width of 373 nm (■), 220 nm (▲) and 94 nm (▼).

rate for low fluence ( $<10^{14} \text{ cm}^{-2}$ ). Further study is needed for a full description of the observed phenomena.

### 3.4 Conclusions

We have shown that silica templates patterned with 45 to 370 nm-wide trenches deform under 6 MeV Au irradiation. The deformation causes a considerable decrease in trench width, while the line-edge roughness of the trenches stays constant. Furthermore, channels that were initially less than 100 nm wide, can close up almost entirely under ion beam irradiation. These results suggest that ion beam irradiation can be an effective technique to miniaturize written features on a substrate.

## **4 Synthesis of gold, silica and gold@silica nanoparticles**

### **4.1 Introduction**

Colloidal particles play an important role in every-day life as well as in many different research areas. The typical size of colloids ranges from a few nm to several  $\mu\text{m}$ . Colloidal particles can therefore be studied using optical or electron microscopy. Since the momentum of colloidal particles in solution is largely controlled by Brownian motion, they are ideal study objects for self-assembly and phase behavior. The optical properties of colloidal particles are also very interesting and studied extensively in various fields of research. Metal nanoparticles have special optical properties, which are partly due to localized surface plasmons. For Au and Ag nanoparticles the plasmon resonance frequencies lie in the visible part of the spectrum [21]. A linear array of these particles can serve as a waveguide for surface plasmons [9]. Au nanoparticles with diameters of 10-100 nm can be made by wet-chemical synthesis [21]. These particles can be coated with a dielectric material, like silica, which can serve as a spacer-layer when the Au particles are aligned in an array. Au particles with a diameter of about 50 nm and a shell-thickness of 10-20 nm are well suited for use in plasmon waveguides, because of the relatively low propagation loss in this case.

In this chapter is described how we have prepared dispersions of Au and Au-core/silica-shell nanoparticles with these dimensions. Furthermore, the synthesis of silica nanoparticles is discussed, as these particles were used to study template-induced colloidal self-assembly.

### **4.2 Silica nanoparticles**

The preparation of silica nanoparticles through hydrolization of silicon alkoxides [tetramethoxy silane (TMOS), tetraethoxy silane (TEOS)] has received considerable attention in the literature [22-27]. In 1968 Stöber *et al.* reported about the hydrolization and polycondensation of TEOS to form amorphous silicate particles [23]. Much work has been done since, in order to find ways to control the monodispersity and incorporate dyes into the particles [22, 27-33]. Using reverse (water-in-oil) micelles it has been demonstrated that nanosized silica particles with

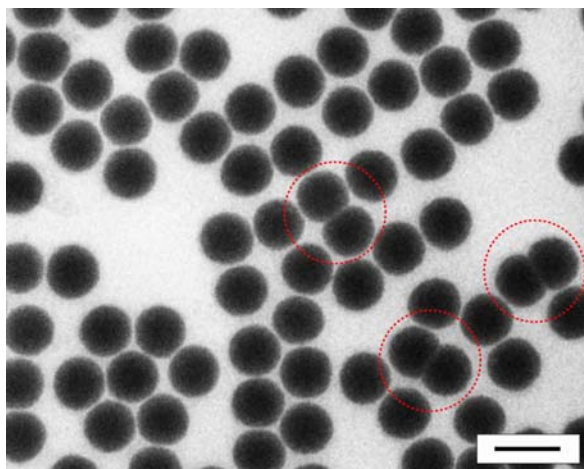


**Figure 4-1:** TEM image of SiO<sub>2</sub> particles after microemulsion synthesis. Average particle diameter is  $81 \pm 2$  nm. Scale bar is 100 nm. Dumbbells are highlighted by the circles.

very low polydispersity can be prepared [34]. We have used this method to synthesize SiO<sub>2</sub> particles that were later used for self-assembly.

A microemulsion was formed at room temperature by addition of 5.1 mL ammonia solution (Merck, 28 wt.%) to a mixture containing 49 mL Igepal CO-520 (Aldrich, p.a.) and 950 mL cyclohexane (Baker, p.a.).

This was slowly stirred for one hour at a constant temperature of 19.5 °C. The synthesis reaction was initiated by addition of 5.9 mL TEOS (Fluka) to the microemulsion. The mixture was allowed to stand for a week, after which cyclohexane was removed by rotary evaporation. The silica particles that had formed in the reverse micelles had a size of ~40 nm. Next, 10 mL dimethyl formamide (Merck, p.a.) and 250 mL ethanol (Merck, p.a.) were added to form a stable dispersion in ethanol. While stirring, another 220 mL ethanol was added coincidentally with 30 mL ammonia solution. Subsequently a volume of 12 mL TEOS was added to the dispersion. After continuous stirring for several days, the particles were centrifuged at 1000 rpm and redispersed in ethanol. Samples for transmission electron microscope (TEM) analysis were obtained by dipping Formvar-covered carbon-coated copper grids into the dispersion and drying at room temperature. TEM was performed at 100 or 120 kV using a Philips Tecnai 10 or 12 transmission electron microscope.

A TEM image of the silica nanoparticles after synthesis is shown in Fig. 4-1. The particles are spherically shaped and have an average diameter of  $81 \pm 2$  nm (3 % polydispersity). About 2-3 % of the particles are dumbbells (highlighted in the image), which are formed when single particles merge during synthesis. The particle

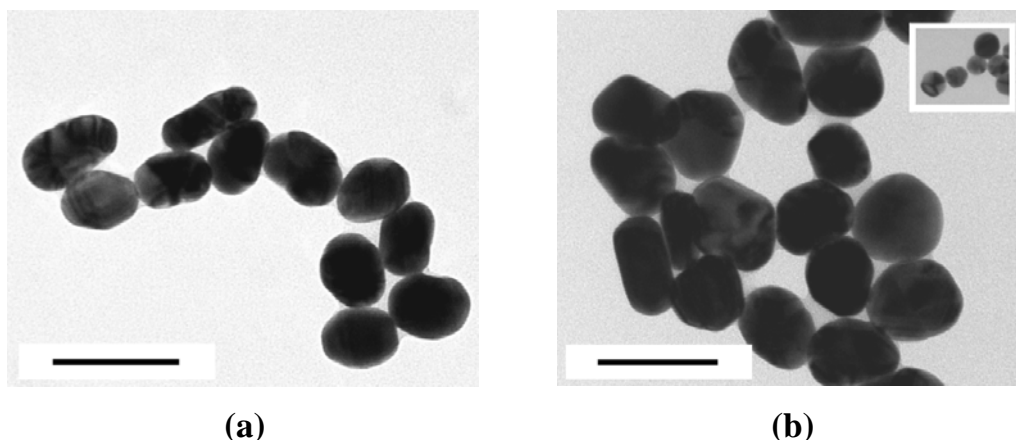


**Figure 4-2:** Au particles formed by citrate reduction. **(a)** Particles prepared in a single reduction. **(b)** Particles prepared by seeded growth, using 15-nm-diameter seeds (shown in inset at same scale). Scale bars are 100 nm.

concentration, determined by drying an amount of the dispersion and weighing the residue, was  $2 \times 10^{15}$  particles  $\text{mL}^{-1}$ .

### 4.3 Gold nanoparticles

Many different methods have been reported for the synthesis of spherical Au nanoparticles [21]. Most of these preparations are based on the reduction of  $\text{Au}^{3+}$  to form colloidal Au. The most widely studied reductant is sodium citrate, which can be used to synthesize Au particles with a diameter of 10 to 150 nm [35]. For large particles ( $>30$  nm) the monodispersity and ellipticity of the particles become very poor, however. It is reported that the monodispersity of these particles can be improved by seeded growth of small ( $\leq 15$  nm), monodisperse Au seeds [36]. We have synthesized Au colloids both by direct reduction and by seeded growth.

Aqueous dispersions of colloidal Au were formed by addition of a 1 wt.% sodium citrate solution (Aldrich, p.a.) to a stirred solution of boiling 0.01 wt.%  $\text{HAuCl}_4$  (Acros Organics, p.a.) in water. All glass was cleaned thoroughly before each synthesis reaction, using HF (8 wt.%) and aqua regia. Au dispersions with different particle diameters were prepared by varying the added amount of citrate. A larger citrate/Au ratio results in smaller particles. After 30 minutes all  $\text{Au}^{3+}$  had been reduced and heating of the solution was stopped. For seeded growth, sodium citrate was added coincidentally with the addition of seed colloids (15-nm-diameter) to the boiling solution of  $\text{HAuCl}_4$ . Particles were characterized using TEM.

**Table 4-I:** Physical properties and process details for Au dispersions prepared by direct citrate reduction and by seeded growth.

synthesis method	batch <sup>a</sup>	citrate/Au ratio <sup>b</sup>	long axis $\times$ short axis <sup>c</sup>	$G$ <sup>d</sup>
direct reduction	1	7.3	16.2 (2.3) $\times$ 14.4 (1.6)	1.13
	2	7.4	19.3 (2.2) $\times$ 17.4 (2.2)	1.11
	3	1.3	46.5 (6.7) $\times$ 34.9 (4.2)	1.33
	5	1.1	62.8 (7.7) $\times$ 46.2 (4.7)	1.36
seeded growth	6	0.6	77.1 (9.4) $\times$ 58.4 (6.7)	1.32
	7	0.7	88.4 (13.5) $\times$ 63.5 (6.9)	1.39

<sup>a</sup> Batch 6 was prepared using seeds from batch 1; batch 7 was prepared using seeds from batch 2. <sup>b</sup> Values are given in mole citrate per mole Au<sup>3+</sup>. <sup>c</sup> Values in parentheses are standard deviations; all values are in nm. <sup>d</sup> Ellipticity, i.e. ratio between long and short axis.

Two typical examples of the different syntheses are shown in Fig. 4-2. The particles in Fig. 4-2a were prepared in a single reaction and had an average size of ~55 nm. Figure 4-2b shows particles that were grown to a size of ~65 nm, using 15-nm-diameter seeds, which are shown in the inset. Table 4-I gives an overview of particle size, ellipticity  $G$  (ratio between the long and short axis) and process parameters for several Au dispersions prepared by reduction with sodium citrate. Although particles, prepared via seeded growth had a larger mean diameter, they were more spherical than particles with a comparable size, prepared by direct reduction (see for example Fig. 4-2). This suggests that Au particle ellipticity can indeed be improved using seeded growth.

#### 4.4 Gold@silica nanoparticles

Coating of surfaces with silica has received a considerable amount of attention since the 1950s [37-44]. Many aspects of colloidal particles can be manipulated with a coating, including the solubility in various solvents and the interaction potential. Furthermore, a silica-shell allows for controlled placement of various dyes and can act as a spacer layer between embedded particles. In the early researches, silica-coatings involved surfaces with an appreciable chemical or electrostatic affinity for silica. Gold has very little affinity for silica, however, mainly because it does not form a

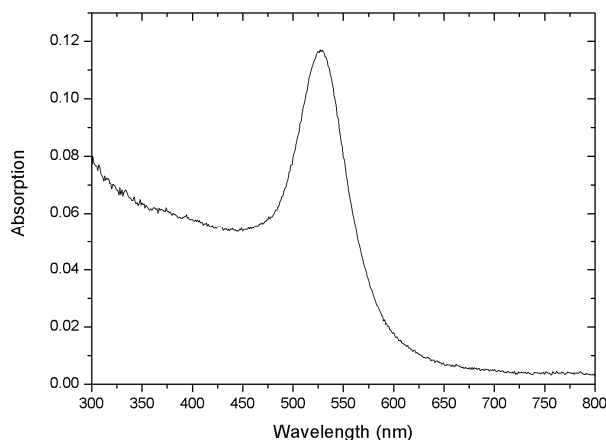


**Figure 4-3:** Absorption spectrum of spherical Au particles in water with an average diameter of 43.9 nm.

passivating oxide layer in solution, unlike other metals. It was only until 1996 that Liz-Marzán *et al.* found a way to grow silica-shells on Au particles. Their method involved the modification of the particle surface by treatment with an amine-terminated silane coupling agent. The coupling agent functions as a primer for subsequent

formation of SiO<sub>2</sub> at the particle surface. Since then, several new methods have been reported involving the use of other silane coupling agents, stabilizers or surfactants [41, 45]. Recently, several methods have been reported to coat colloidal Au without the use of primers [42, 43]. Lu *et al.* reported about a procedure to coat 50-nm Au particles homogenously with ~20 to 100 nm-thick silica-shells [43]. They showed that the overall synthesis is much faster, because the Au surface does not need to be modified. However, they did not investigate the growth mechanism in detail.

We have used this method to synthesize Au-core/SiO<sub>2</sub>-shell particles. Spherical Au particles with an average diameter of  $43.9 \pm 3.7$  nm were obtained from Ted Pella (Redding, CA). A Perkin Elmer Lambda 16 UV/Vis spectrometer was used to measure the optical absorption spectrum, in order to determine the particle concentration in dispersion. Figure 4-3 shows the absorption spectrum of the Au colloids (11x diluted in water). An absorption maximum is observed at a wavelength of 527 nm which is in good agreement with the surface plasmon resonance wavelength for nanoparticles of this size in water. Using a calculated absorption coefficient of  $3.7 \times 10^{-11} \text{ cm}^2$  (for 45-nm-sized particles) a particle concentration of  $3.3 \times 10^{10} \text{ ml}^{-1}$  was found.

In a typical synthesis, 2 mL of the Au dispersion (used as received) was added to 10 mL 2-propanol (Baker, p.a.). Under continuous stirring, 0.25 mL ammonia solution (Fluka, 28 wt.%) and various amounts of TEOS (Fluka, p.a.) dissolved in 2-

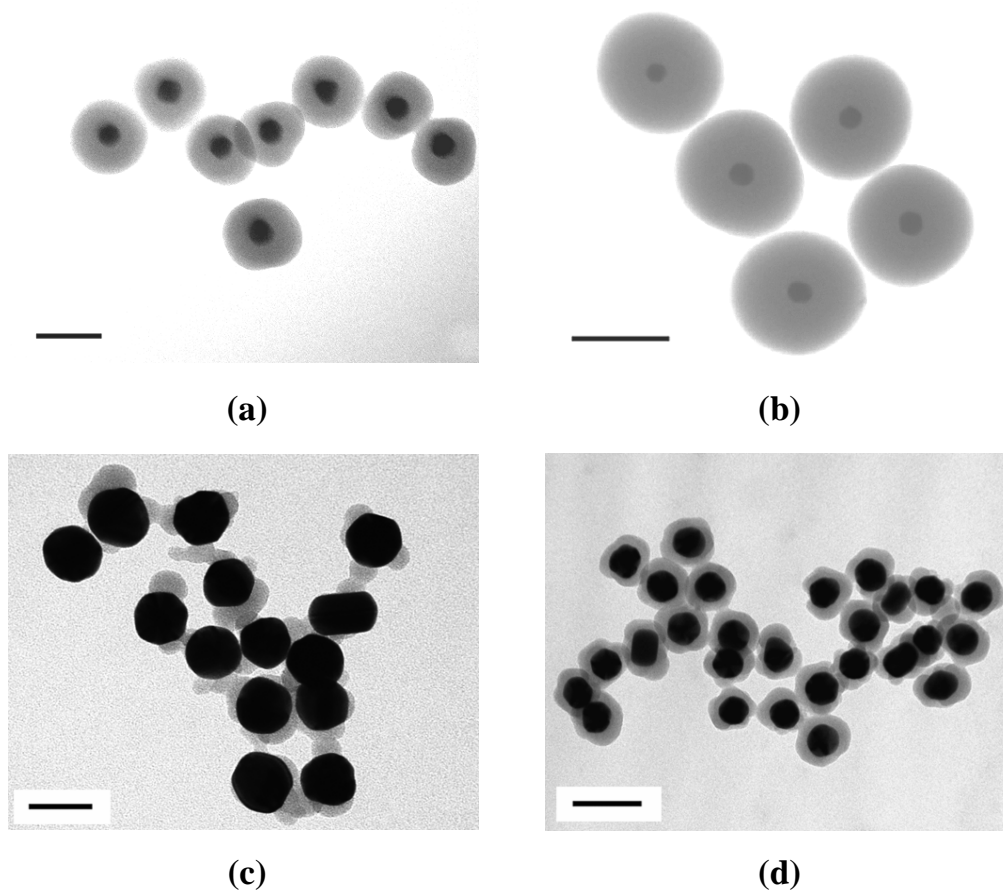


**Figure 4-4:** TEM images of Au-core/SiO<sub>2</sub>-shell particles with an average core diameter of 43.9 nm and different shell-thickness. Added amount of TEOS solution: (a) 50  $\mu$ L; (b) 500  $\mu$ L; (c) 25  $\mu$ L; (d) 50  $\mu$ L (to 15 $\times$  concentrated Au dispersion). Scale bars are: (a) 100 nm; (b) 200 nm; (c) 50 nm; (d) 100 nm.

propanol (to a concentration of 2 vol.%) were added to the dispersion. After stirring for approximately 2 hours at room temperature, the particles were centrifuged at 3000 rpm and redispersed in ethanol. Characterization of the particles was done using TEM.

Several TEM images of Au-core/silica-shell particles are shown in Fig. 4-4. While particles could reproducibly be coated with thick (>50 nm) shells, synthesis of thinner shells was not straightforward. In case less than 50  $\mu$ L of the TEOS solution is added to the Au dispersion, the shells do not form homogeneously (Fig. 4-4c) or all silica is formed as second nucleation. From TEM images, it appears that silica nucleates very slowly at the surface of the Au nanoparticles at these low TEOS concentrations. Above a threshold of  $\sim$ 50  $\mu$ L, silica-shells are formed with a homogeneous thickness

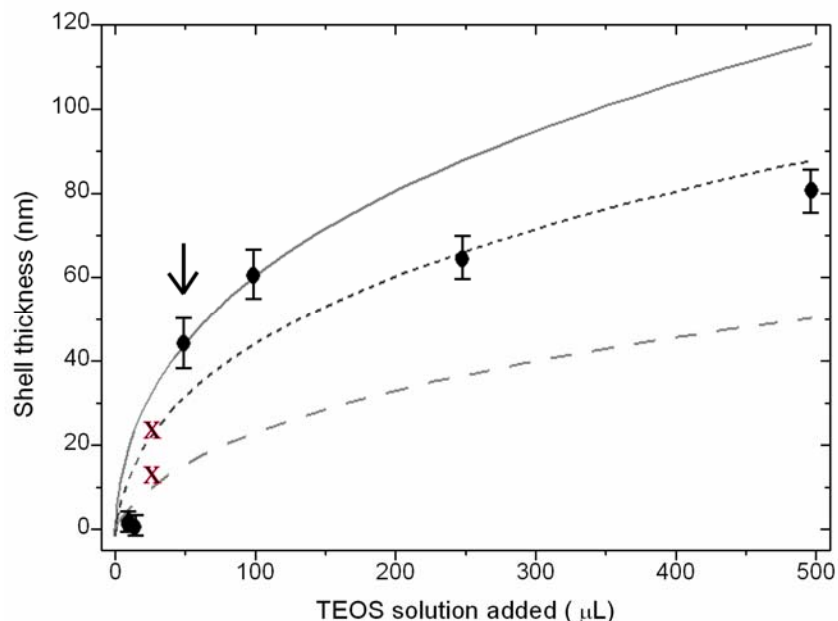


**Figure 4-5:** Shell-thickness as a function of TEOS solution added to the Au dispersion. The black dots are measured from TEM images. The curves are theoretical predictions of the shell-thickness. Solid curve: no second nucleation; dotted curve: 50% second nucleation; dashed curve: 15× concentrated Au dispersion, no second nucleation. The two crosses in the figure represent particles with a very inhomogeneous shell (see for example Fig. 4-4c). The arrow indicates the TEOS solution threshold of 50  $\mu\text{L}$ . Above this value homogenous shells are formed.

of at least 50 nm (Fig. 4-4a and b). Very little second nucleation (i.e. silica that is not deposited on the Au particles) is formed in case 50-100  $\mu\text{L}$  TEOS solution is added. At higher TEOS concentrations, the amount of second nucleation increases. This is illustrated in Fig. 4-5, in which the shell-thickness is plotted vs. the amount of TEOS solution added. Given the Au particle concentration and the molar volumes of TEOS and silica we could calculate the expected thickness of the silica shell as a function of added TEOS. When we assume all the silica is deposited on the Au nanoparticles (no second nucleation), the shell-thickness is predicted by the solid curve in the figure. This curve intersects with the first two points above the threshold, which agrees with observations. The dotted curve in Fig. 4-5 gives the expected shell-thickness in case 50 % of the silica is formed as second nucleation.

As we were not able to coat Au particles with shells of the aimed thickness (10-20 nm) this way, we have tried to modify the synthesis slightly. First, we have studied the effect of using a more highly concentrated Au dispersion. We expected this would lead to the formation of thinner shells, as the deposition of silica would be divided over a larger number of particles. The shell-thickness was calculated for a Au dispersion that was concentrated  $15\times$  (dashed line in Fig. 4.5). At the threshold (50  $\mu\text{L}$  TEOS solution) this curve predicts a shell-thickness  $<20$  nm. Figure 4-4d shows a TEM image of single particles with a  $\sim 15$  nm-thick shell that were prepared by addition of 50  $\mu\text{L}$  TEOS solution to a  $15\times$  concentrated Au dispersion. However, besides the formation of single particles, most of the Au particles had clustered into large Au-silica aggregates. The single particles could be separated from the aggregates by centrifugation. Core-shell particles of Au and silica can thus be prepared with a small shell-thickness, though at a high loss of Au particles.

Another experiment that was carried out to achieve coating of Au with thinner silica-shells, was by addition of micrometer-sized  $\text{SiO}_2$  seeds to the Au dispersion prior to the addition of TEOS. As this increases the total deposition surface, it has a limiting effect on the amount of silica deposited on the Au colloids, possibly resulting in thinner silica-shells. After addition of 10  $\mu\text{L}$  of a seed dispersion in ethanol ( $\varnothing = 1.0$   $\mu\text{m}$ , 7 g  $\text{SiO}_2/\text{L}$ ) we carried out the synthesis with 100 and 150  $\mu\text{L}$  of the TEOS solution. Unfortunately, this approach led to inhomogeneous coatings, comparable to those shown in Fig. 4-4c. This suggests that nucleation on the Au-surface is the limiting step in the reaction, as most silica is deposited on the  $\mu\text{m}$ -sized silica colloids, even though their total surface was smaller than the total surface of the Au particles.

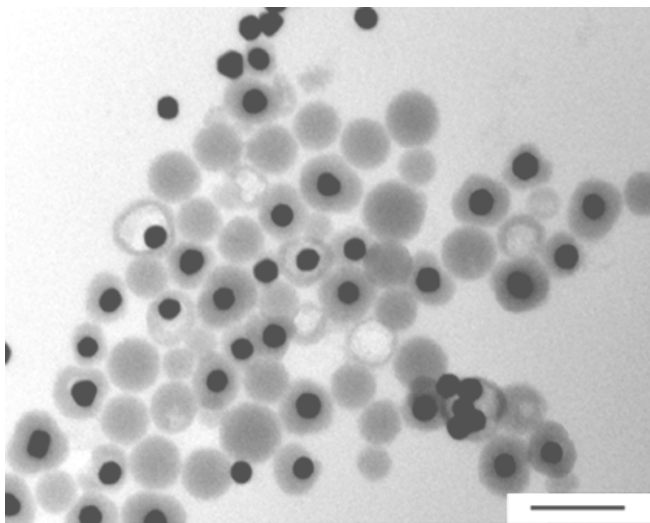


**Figure 4-6:** TEM image of Au-core/SiO<sub>2</sub>-shell particles after they had been in demineralized water for eight days. Scale bar is 200 nm.

Another approach to get thin homogeneous silica shells is by dissolving the shell in water. We have tried this for particles with an initial shell-thickness of ~50 nm that were redispersed in demineralized water (18 MΩ). The amount of second nucleation before the experiment was about 50 %. A TEM image of the particles after they had been in the water for a period of

eight days is shown in Fig. 4-6. Some of the particles seemed to have lost their entire shell, while others were trapped inside hollow spheres of silica. The image shows that silica can be dissolved in water and that shells can be dissolved from inside out. This suggests that water can diffuse through the shell, which means that the shells are quite porous.

Finally it should be pointed out that shells with any desired thickness can possibly be made if the deposition of silica on the Au particles can be stopped anytime during the reaction. This might be done by addition of particles that compete in the silica-shell formation, or by addition of HCl to diminish the catalytic effect of the ammonia. This will be further investigated.

## 4.5 Conclusions

Three types of colloidal particles have been prepared: monodisperse silica spheres ( $\varnothing \sim 80$  nm), ellipsoidal Au particles ( $\varnothing \sim 15$ -70 nm), and spherical particles with a Au core ( $\varnothing \sim 45$  nm) and silica-shell ( $\varnothing \sim 15$ -80 nm). Several of these particles were later used in self-assembly experiments. It has been shown that the ellipticity of large Au particles ( $>30$  nm) can be decreased slightly, when the synthesis is carried out with small spherical Au seeds ( $\varnothing \sim 15$  nm). Furthermore, it has been shown that Au

particles can be coated with thick ( $>50$  nm) silica-shells, without the use of any surfactant or primer. Synthesis of thinner shells is more difficult however, because homogeneous shells are only formed above a certain TEOS-concentration threshold. Thin silica-shells could, however, be successfully grown on Au colloids in a highly concentrated dispersion, although at high loss of Au. Both the addition of silica particles that compete in the silica-shell formation and the attempt to dissolve the shells in water, did not give satisfactory results. Formation of thinner shells will be further investigated with experiments in which the reaction is allowed to proceed for short periods of time, after which the silica-nucleation on the Au particles is terminated.

## 5 Template-assisted self-assembly of nanoparticles

### 5.1 Introduction

Colloidal nanoparticles are becoming more and more promising as building units for nanotechnology, as conventional lithographic approaches are approaching fundamental limits. For fabrication of devices, precise control over particle positioning is of vital importance. With template-assisted self-assembly - an integration of lithography and self-assembly - particles can be assembled at precise locations, defined by the template. Typically, this is done by drying a colloidal dispersion on a template. Evaporation of the solvent leads to the three-phase contact line moving slowly across the substrate. Particles in the rear edge of the liquid slug experience a capillary force, which pushes the particles into the lithographically defined features, where they are physically trapped. This is schematically illustrated in Fig. 5-1a. The movement of particles is further governed by an electrostatic force, which can be either repulsive or attractive, depending on the signs of charges on the surfaces of the particles and templates, and a gravitational force, which is generally much smaller than the capillary force. Furthermore, colloidal particles undergo Brownian motion which complicates the self-assembly. Another effect of the capillary force is illustrated in Fig. 5-1b. As the solvent evaporates individual particles are pushed together as a result of the total capillary force exerted on the particles by the

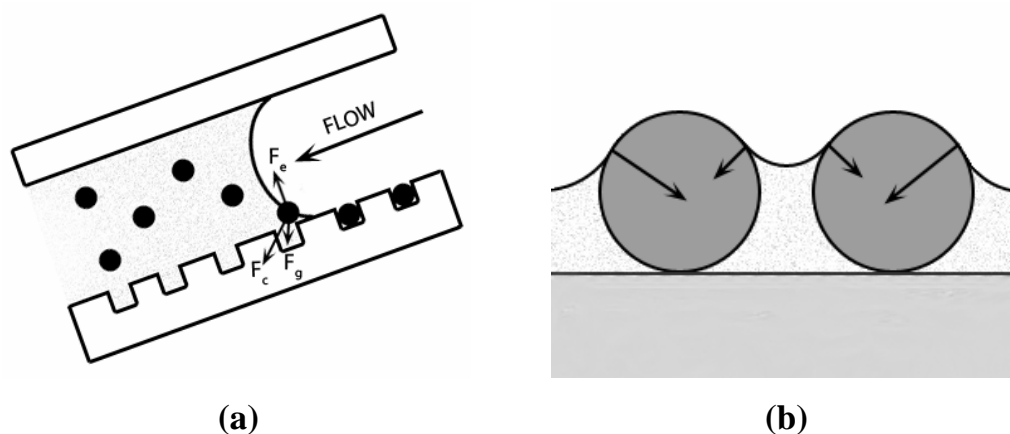


**Figure 5-1:** Schematics, illustrating the self-assembly process. **(a)** Cross-sectional view of a flow-cell, showing the three forces governing the self-assembly process. **(b)** Illustration showing the capillary forces for two particles close together upon evaporation of the solvent. As the attractive force is greater than the repulsive force, the two particles will be pushed together.

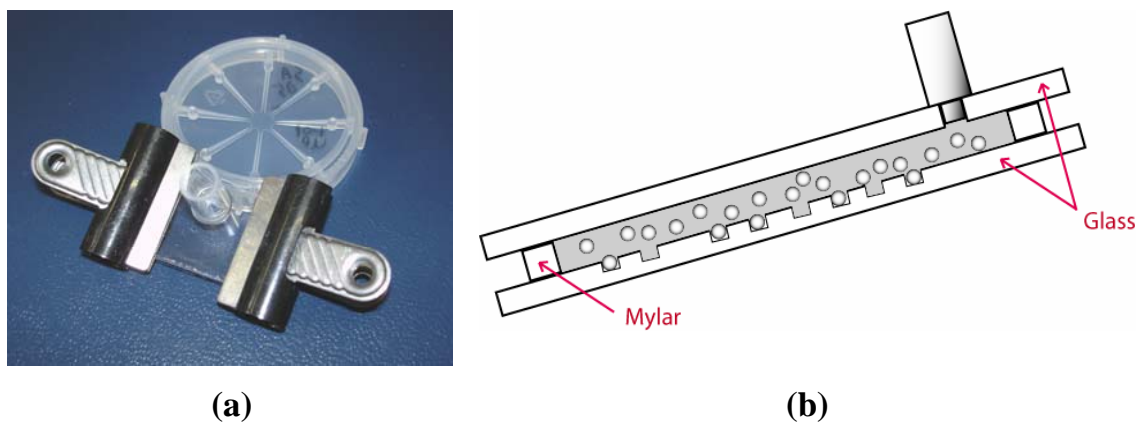


**Figure 5-2:** Images of the flow-cell used in the procedure to form self-assembled arrays of particles. **(a)** Photograph of assembled flow-cell. **(b)** Cross-sectional schematic view of the flow-cell.

solvent-vapor interface.

This chapter describes self-assembly experiments involving the previously discussed templates (Chapter 2) and colloidal nanoparticles (Chapter 4).

## 5.2 Silica nanoparticles

Silica colloids were self-assembled inside trenches using a controlled flow-cell, shown in Fig. 5-2a [46]. The cell consisted of two glass substrates, sandwiching a 35- $\mu\text{m}$ -thick Mylar frame (Dupont Teijin Films, Luxembourg). The pattern was contained on the bottom substrate, while the colloidal dispersion was supplied through a hole ( $\varnothing \sim 2 \text{ mm}$ ) in the top substrate. A hollow tube ( $\varnothing \sim 5 \text{ mm}$ ) was glued onto the substrate to allow for easy addition of the dispersion. The cell was tightened using binder clips. A Mylar frame was cut with scissors and cleaned with acetone. The frame was subsequently scratched with a soft tissue to create evaporation channels for the liquid [47]. The Mylar-frame thus served both as a spacer between the two glass substrates and as a barrier to control the rate at which the dispersion flowed through the cell. A schematic representation of self-assembly in the cell is shown in Fig. 5-2b.

After the flow-cell had been assembled, a dispersion of 80-nm-diameter silica nanoparticles in ethanol ( $3\times$  redispersed in ethanol; see Chapter 4.2 for synthesis details) was injected into the cell through the glass tube. Once the dispersion had completely filled the space between the bottom and top substrate of the cell, the excess liquid was removed from the tube using a syringe. Next, the tube was closed

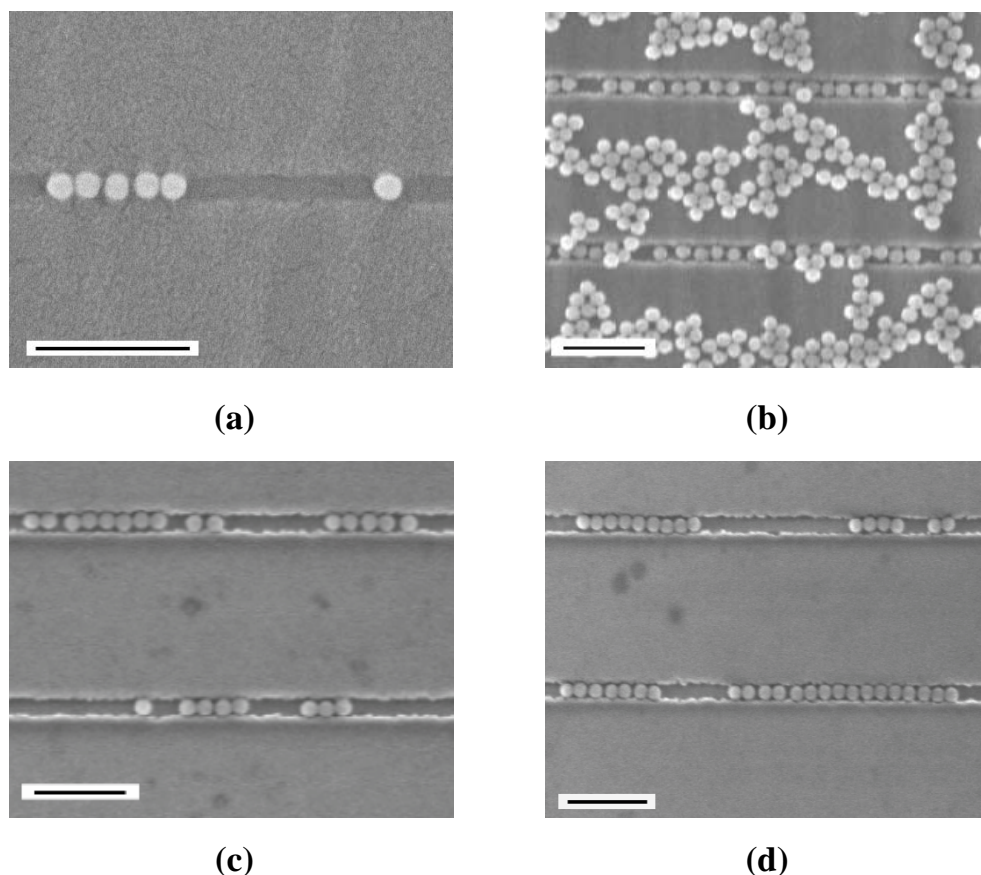


**Figure 5-3:** SEM images of self-assembled silica particles on silica templates. **(a)** Using a dispersion with a relatively low particle concentration ( $5 \times 10^{14} \text{ mL}^{-1}$ ). **(b)** Using a dispersion with a relatively high particle concentration ( $1 \times 10^{15} \text{ mL}^{-1}$ ). **(c)** Sample from (b) after 60 minutes sonication in water. **(d)** Sample from (b, c) after  $3 \times$  self-assembly and subsequent sonication. Scale bars are 500 nm.

off using Parafilm and the liquid was allowed to evaporate from the cell, which was slightly tilted to an angle of about  $30^\circ$ . The drying time was typically several hours.

The sample was subsequently studied using SEM. Images are shown in Fig. 5-3. Drying of dispersions with relatively low particle concentrations ( $5 \times 10^{14} \text{ mL}^{-1}$ ) resulted in the formation of several arrays of 2-5 particles in the trenches (Fig. 5-3a). Hardly any particles were found on the substrate between the trenches. This was very different in case a more concentrated dispersion ( $1 \times 10^{15} \text{ mL}^{-1}$ ) was used for the experiment. In this case, particle aggregates were formed all over the sample and not just inside the trenches (Fig. 5-3b). Particle arrays of up to  $\sim 10$  particles were formed in the trenches, however.

In order to remove the excess particles on the substrate in-between the trenches, the sample was sonicated in water for 60 minutes (Branson 2510, 130 W). The results of this treatment are shown in Fig. 5-3c. Most of the particles on the substrate have been removed because of the treatment, while particles inside the trenches were hardly affected. In order to further improve on these results, we have repeated previous steps (i.e. self-assembly followed by sonication) several times. As a result, somewhat longer arrays of up to ~15 particles were formed inside the trenches (Fig. 5-3d).

### 5.3 Gold nanoparticles

Self-assembly of uncoated Au particles was studied with vertical drying [48]. An aqueous Au dispersion (Ted Pella, ~44 nm,  $3 \times 10^{10} \text{ mL}^{-1}$ ) was dried over a template at a constant temperature of 60°C. The process is illustrated in Fig. 5-4a. The template was tilted to an angle of 30° during the experiment. It generally took about two hours before all of the solvent had been evaporated.

SEM images of the sample after drying are shown in Fig. 5-4b-d. A photograph of the sample after drying (Fig. 5-4b) shows a collection of horizontal purple stripes where gold had been deposited on the sample. The SEM images in Fig. 5-4c-d show one of these stripes in more detail. The individual stripes are made up of fractal-like structures, consisting of nearly parallel lines that do not cross anywhere. In general, hardly any gold had deposited in-between the stripes. This suggests that Au only precipitates above a certain threshold concentration. Each precipitation leads to a drop in the particle concentration below the threshold. After some time the concentration reaches the threshold again and another stripe is formed. This continues until the solvent has completely evaporated.

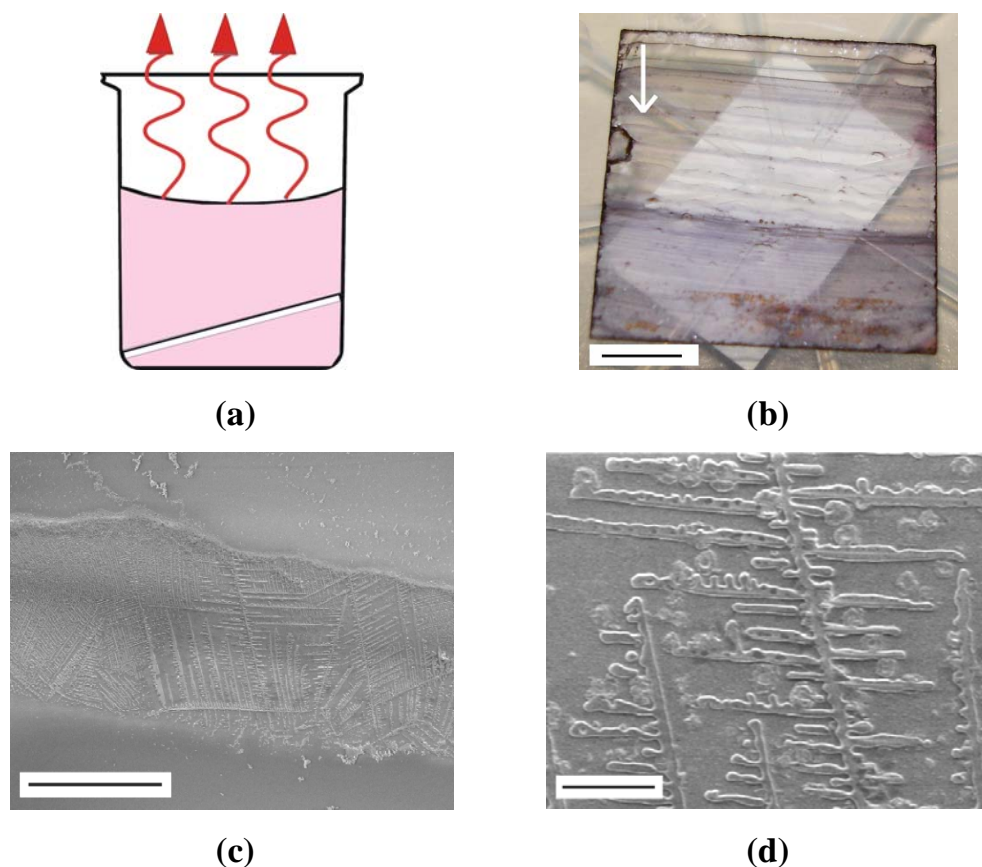


**Figure 5-4:** (a) schematic illustration of the drying technique used to create self-assemblies of Au nanoparticles. Solvent temperature was kept constant at 60°C. (b) Photograph of sample after drying. The arrow indicates the change of fluid level during evaporation. (c) SEM image of sample, showing one of the horizontal stripes where gold had been deposited. (d) SEM image showing a detail of the horizontal stripe. Scale bars are: (b) 5 mm; (c) 200  $\mu\text{m}$ ; (d) 20  $\mu\text{m}$ .

Deposition of Au particles over line-patterns and hole-patterns has been investigated. Various SEM images of Au assemblies after drying are shown in Fig 5-5. Figure 5-5a shows several writing fields just outside a precipitation region (stripe). A close-up of one of the fields (marked by the circle), is shown in Fig. 5-5b. At this field, Au particles have self-assembled into arrays of two or three particles. Only short arrays had formed, because the trenches were too narrow for the particles at most places. The deposited Au particles had not coagulated in the trenches and were not deposited on the substrate in-between the trenches.

However, at the precipitation areas individual particles could not be distinguished. Figure 5-5c shows that  $\mu\text{m}$ -long nanowires can be formed in case Au precipitates over a line pattern. This indicates that the shapes of objects formed during precipitation can be influenced by the template. Several Au particles did not melt and join with other

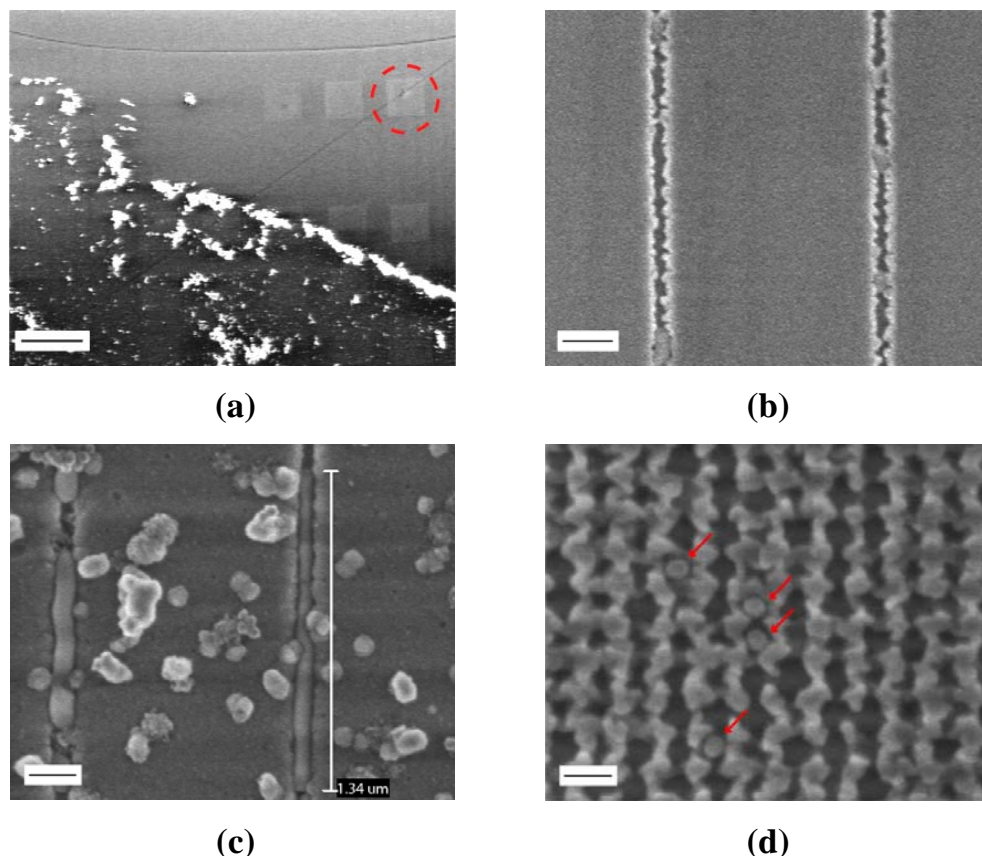


**Figure 5-5:** SEM images of Au nanostructures on silica templates. **(a)** E-beam patterned fields just outside a precipitation region. The circle marks the field that is shown in close-up in Fig. 5-5b. **(b)** Au particle assemblies inside channels at a field outside a precipitation region. **(c)** Coagulated Au structures on a template with channels, inside a Au precipitation region. **(d)** Au particle assemblies at a hole pattern (outside precipitation region). Trapped Au particles are indicated by the red arrows. Scale bars are: (a) 100  $\mu\text{m}$ ; (b) 200 nm; (c) 200 nm; (d) 100 nm.

particles during the precipitation (see the top-left and center part of Fig 5-5c). It is well-known that the melting temperature of nm-sized metal particles can be considerably lower than the bulk melting temperature [49, 50]. As small particles have a relatively high surface to volume fraction, the melting temperature is directly affected by changes in the surface free energy of the metal. Surfactant molecules may therefore also have a strong effect on the melting point of the particles. Further investigation, e.g. comparing with results using citrate-stabilized Au, might give more insight in the melting process. Figure 5-5d shows results of self-assembly in a hole pattern (outside a precipitation area). Only few of the holes are actually filled with Au colloids (indicated by the red arrows), which suggests that the particles are not very tightly trapped by the hole pattern.

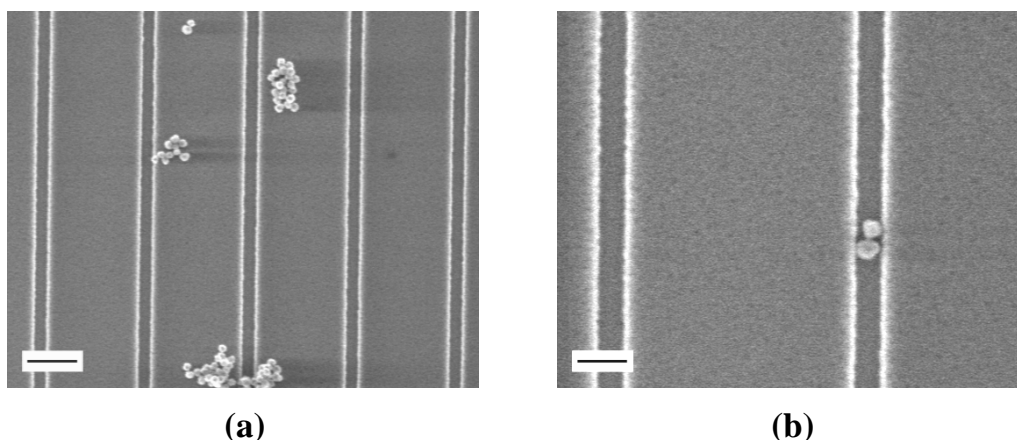


**Figure 5-6:** SEM images of Au-core/silica-shell assemblies on silica templates. Scale bars are (a) 500 nm; (b) 100 nm.

## 5.4 Gold@silica nanoparticles

Preliminary experiments of self-assembly of Au-core/silica-shell nanoparticles were performed using a flow-cell and the procedure described in Chapter 5.2. We used particles with a  $\sim 44$  nm core and a  $\sim 15$  nm shell (Fig. 4-4d). Figure 5-6 shows that the particles do not self-assemble preferentially in the trenches, but rather form aggregates of about 2-10 particles all over the substrate. This behavior needs to be further investigated.

## 5.5 Conclusions

Self-assembly has been investigated for silica, gold and gold-core/silica-shell nanoparticles on silica templates. Using a flow-cell, 80-nm-sized silica particles could be assembled in trenches to form arrays of up to  $\sim 15$  particles. Excess particles on the substrate could be removed by sonication, after which the self-assembly process could be repeated to make longer arrays. Drying of a Au dispersion over a silica template at  $60^\circ\text{C}$  caused a macroscopic precipitation of gold particles. Investigation of the precipitated gold shows that the individual particles had coagulated and changed shape. The shape of objects formed was influenced by the template. In case Au precipitates over a line pattern, the particles can coagulate to form  $\mu\text{m}$ -long nanowires in the trenches. Preliminary experiments with Au-core/silica-shell nanoparticles suggest that these particles do not preferentially self-assemble into the defined pattern, but rather form aggregates everywhere on the substrate. This behavior needs to be investigated in more detail.

## ***Acknowledgements***

The work in this thesis was carried out at the FOM-institute Amolf in Amsterdam and at the University of Utrecht. Templates were prepared at the Amsterdam Nanocenter. I would like to thank Chris R  tif in particular for his help with the nanofabrication. All colloidal synthesis was done at the Soft Condensed Matter group of Alfons van Blaaderen in Utrecht. Alfons, Carlos, Carmen and Dannis, thank you very much for all your help! While in Utrecht, I would also like to thank Arjen Vredenberg for his help with the ion-beam irradiation. At Amolf, my gratitude furthermore goes to all the members of the Photonic Materials group: Anna, Ewold, Hans, Jan, Jeroen, Martien, Rob, Timon and especially to my supervisors Joan Penninkhof and Albert Polman.

### Reference list

- [1] B. E. A. Saleh and M. C. Teich, *Fundamentals of Photonics*, Wiley, New York **1991**.
- [2] A. Mekis, J.C. Chen, I. Kurland, S. Fan, P. R. Villeneuve, and J. D. Joannopoulos, *Phys. Rev. Lett.* **1996**, 77, 3787.
- [3] J. Moosburger, M. Kamp, A. Forchel, S. Olivier, H. Benisty, C. Weisbuch, and U. Oesterle, *Appl. Phys. Lett.* **2001**, 79, 3579.
- [4] M. Quinten, U. Kreibig, *Appl. Opt.* **1993**, 32, 6173.
- [5] B. Lamprecht, J. R. Krenn, G. Schider, H. Ditlbacher, M. Salerno, N. Felidj, A. Leitner, F. R. Aussenegg, and J. C. Weeber, *Appl. Phys. Lett.* **2001**, 79, 51.
- [6] J. C. Weeber, A. Dereux, C. Girard, J. R. Krenn, and J. P. Goudonnet, *Phys. Rev. B* **1999**, 69, 9061.
- [7] R. M. Dickson, and L. A. Lyon, *J. Phys. Chem. B* **2000**, 104, 6095.
- [8] U. Kreibig, and M. Vollmer, *Optical properties of metal clusters*, Springer, Berlin **1995**.
- [9] M. Quinten, A. Leitner, J. R. Krenn, and F. R. Aussenegg, *Opt. Lett.* **1998**, 23, 1331.
- [10] S.A. Maier, P. G. Kik, H. A. Atwater, S. Meltzer, E. Harel, B. E. Koel and A. A. G. Requicha, *Nature Mater.* **2003**, 2, 229.
- [11] M. L. Brongersma, J. W. Hartman, and H. A. Atwater, *Phys. Rev. B* **2000**, 62, R16356.
- [12] S. A. Maier, P. G. Kik and H. A. Atwater, *Appl. Phys. Lett.* **2002**, 81, 1714.
- [13] N. Silvis-Cividjian, C. W. Hagen, P. Kruit, M. A. J. van de Stam and H. B. Groen, *Appl. Phys. Lett.* **2003**, 82, 3514.
- [14] L. Cartz, F. G. Karioris and R. A. Fournelle, *Radiat. Eff.* **1981**, 54, 57.
- [15] S. Klaumünzer and G. Schumacher, *Phys. Rev. Lett.* **1983**, 51, 1987.
- [16] S. Klaumünzer, Changlin Li and G. Schumacher, *Appl. Phys. Lett.* **1987**, 51, 97.
- [17] M.-d. Hou, S. Klaumünzer and G. Schumacher, *Phys. Rev. B* **1990**, 41, 1144.
- [18] A. Benyagoub, S. Löffler, M. Rammensee, S. Klaumünzer and G. Saemann-Ischenko, *Nucl. Instrum. Methods Phys. Res. B* **1992**, 228, 65.

- [19] T. van Dillen, P. Onck, E. van der Giessen and A. Polman, *Phys. Rev. B* **2005**, 71, 24103.
- [20] E. Snoeks, A. Polman and C. A. Volkert, *Appl. Phys. Lett.* **1994**, 65, 2487.
- [21] M-C. Daniel and D. Astruc, *Chem. Rev.* **2004**, 104, 293.
- [22] C. J. Brinker, D. E. Clark and D. R. Ulrich, *Better Ceramics Through Chemistry III* **1988**, Materials Research Society.
- [23] W. Stöber, A. Fink and E. Bohn, *J. Colloid Interface Sci.* **1968**, 26, 62.
- [24] C. J. Brinker, K. D. Keefer, D. W. Schaefer and C. S. Ashley, *J. Non-Cry& Solids* **1982** 48, 47.
- [25] R. A. Assink and B. D. Kay, *J. Non-Cryst. Solids* **1988**, 99, 359; **1988**, 104, 112; **1988**, 107, 35.
- [26] B. E. Yoldas, *J. Mater. Sci.* **1979**, 14, 1843; *J. Non-Cry&. Solids* **1986**, 82, 11.
- [27] J. C. Pouxviel, J. P. Boilot, J. C. Beloeil and J. Y. Lallemand, *J. Non-Cry&. Solids* **1987**, 89, 345; **1987**, 94, 374.
- [28] G. H. Bogush, M. A. Tracy, G. L. Dickstein, P. Lee, K. C. Zukoski and C. F. Zukoski, (a) in C. S. Brinker, D.F. Clark and D.R. Ulrich (Eds), Materials Research Society, *Better Ceramics Through Chemistry III* **1988**, p. 57; (b) *J. Non-Cryst. Solids* **1988**, 104, 95.
- [29] T. Matsoukas and E. Gulari, in Y. A. Attia, B. M. Moudgil and S. Chander (Eds), Elsevier, Amsterdam, *Interfacial Phenomena in Biotechnology and Materials Processing* **1988**, p. 149.
- [30] C. H. Byers, M. T. Harris and D. F. Williams, *Ind. Eng. Chem. Res.* **1987**, 26, 1916.
- [31] A. K. van Helden, J. W. Jansen and A. Vrij, *J. Colloid Interface Sci.* **1981**, 81, 354.
- [32] A. P. Philipse and A. Vrij, *J. Chem. Phys.*, **1987**, 87, 5634.
- [33] A. van Blaaderen and A. Vrij, *Langmuir* **1992**, 8, 2921.
- [34] K. Osseo-Asare and F. J. Arriagada, *Colloids and surf.* **1990**, 50, 321.
- [35] G. Frens, *Nature* **1972**, 241, 20.
- [36] K. R. Brown, D. G. Walter and M. J. Natan, *Chem. Mater.* **2000**, 12, 306.
- [37] R. K. Iler, U.S. Patent No. 2, 885366, **1959**.
- [38] M. Ohmori, E. Matijević, *J. Colloid Interface Sci.* **1992**, 150, 594.

- [39] A. P. Philipse, M. P. B. van Bruggen, C. Pathmamanoharan, *Langmuir* **1994**, 10, 92.
- [40] S. Chang, L. Liu, S. A. Asher, *J. Am. Chem. Soc.* **1994**, 116, 6739.
- [41] C. Graf, D. L. J. Vossen, A. Imhof and A. van Blaaderen, *Langmuir* **2003**, 19, 6693.
- [42] E. Mine, A. Yamada, Y. Kobayashi, M. Konno and L. M. Liz-Marzán, *J. Colloid Interface Sci.* **2003**, 264, 385.
- [43] Y. Lu, Y. Yin, Z-Y. Li and Y. Xia, *Nano lett.* **2002**, 2, 785.
- [44] L. M. Liz-Marzán, M. Giersig and P. Mulvaney, *Langmuir* **1996**, 12, 4329.
- [45] M. P. B. van Bruggen, *Langmuir* **1998**, 14, 2245.
- [46] Y. Yin, Y. Lu, B. Gates and Y. Xia, *J. Am. Chem. Soc.* **2001**, 123, 8718.
- [47] Y. Lu, Y. Yin, B. Gates and Y. Xia, *Langmuir* **2001**, 17, 6344.
- [48] Y. Cui, M. T. Björk, J. A. Liddle, C. Sönnichsen, B. Boussert and A. P. Alivisatos, *Nano lett.* **2004**, 4, 1093.
- [49] F. Ercolessi, W. Andreoni and E. Tosatti, *Phys. Rev. Lett.* **66**, 911, 1991.
- [50] R. R. Vanfleet, J. M. Mochel, *Surf. Sci.* **1995**, 341, 40.